

CCD photometry in modern astronomy

Experiment F30

Long report for the Advanced Laboratory Course (FP)

Experiment carried out on the 28.09.2020

Report handed in on the 13.10.2020

Supervisor: Grigorii Smirnov-Pinchukov

Maïke Clausen, Celine Beier

Photometry

In general photometry is a part of observational astronomy that considers the spatial distribution of different intensities of light in different wavelengths. Contrasting to spectrometry, the other significant method used in astronomy, photometry does not do a complete Fourier-analysis of the incoming light but differentiates between the wavelengths using filters (U,V,R,I) hence limiting the measured light to a band of wavelengths rather than specific wavelengths. We will be using photometry with a visual and an infrared filter to derive point spread functions of data taken by the Hubble Space Telescope of the globular cluster BS90 in the corresponding filters. Using these we will then determine a point spread function model of the data in the respective filters and then crossmatch them to only use the stars found in the V and I data for our Colour-Magnitude-Diagram from which we will derive the distance, age and metallicity.

Photometry is done using so called CCDs (charged-coupled-devices) by connecting them to a Telescope. The setup we will be using is shown in the figure below:

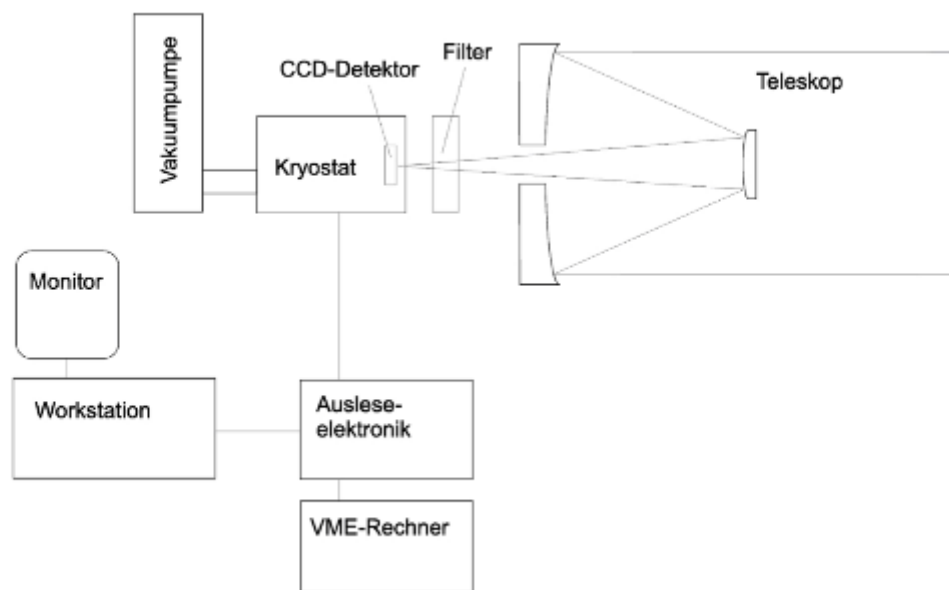


Figure 0: Experimental setup (Source: https://svn.mpia.de/trac/gulli/king/attachment/wiki/WikiStart/FP30Doc/Anleitung_F30.pdf)

In order to get useful astronomical data to perform the photometry different quantities of the CCDs have to be taken into account. Therefore, the first part of the experiment consists of determining those quantities and afterwards the second part focuses on the actual photometry.

Part I: Characterization of the CCD

CCD camera

A CCD camera is based on MOS transistors that function as individual pixels. A MOS (metal-oxide-semiconductor) transistor consists of a doped semiconductor (often silicon is used as it is the most abundant and cheap semiconductor material) that is separated by an insulator layer (most often silicon dioxide) from a conductor material. By applying a voltage to the semiconductor material, a potential well is created below the semiconductor layer. Incident photons are able to excite electrons in the semiconductor material from the valence band into the conduction band and therefore create an electron-hole-pair. Depending on the doping and the applied voltage, either the hole or the electron will move into the semiconductor while the other is collected in the potential well. By modifying the applied voltages the potential well can be deformed in a way that the collected charge carriers can be read out. The number of collected charge carriers will be proportional to the number of incident photons.

Dark Current Measurements

An undesired side effect that will influence the accuracy of the detector is the so-called dark current that is created by the thermal excitation of electrons from the valence to the conduction band. It can be minimised by cooling the detector which will reduce the thermal kinetic energy of the electrons. During the cooling of the detector with liquid nitrogen the dark current was measured as the median of the taken images corrected by the bias values. The bias value was determined as the median from the overscan region and subtracted from the scan region for each picture individually. This is important as the bias values changed during the cooling. For example, the bias value for a temperature of -0.3°C was

$$V_{\text{bias}} = (1439 \pm 11)\text{ADU}$$

whereas the for a temperature of -103.4°C the bias value was only

$$V_{\text{bias}} = (1345 \pm 2)\text{ADU}$$

The median value of the bias as well as its scatter change from image to image but both decrease with decreasing temperature as the effect of thermal excitation diminishes. The results for the dark current measurement are shown in figure 1.

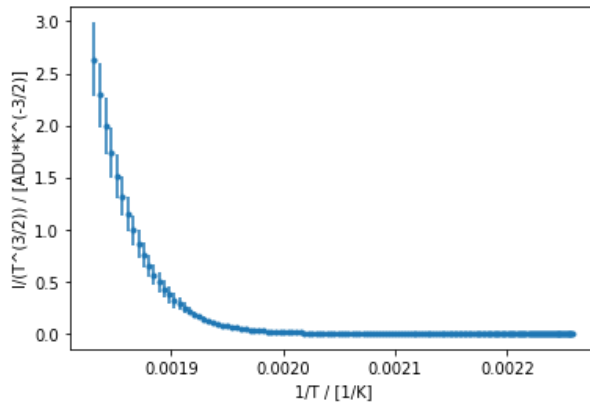


Fig.1: Dark Current Measurement, linear scale

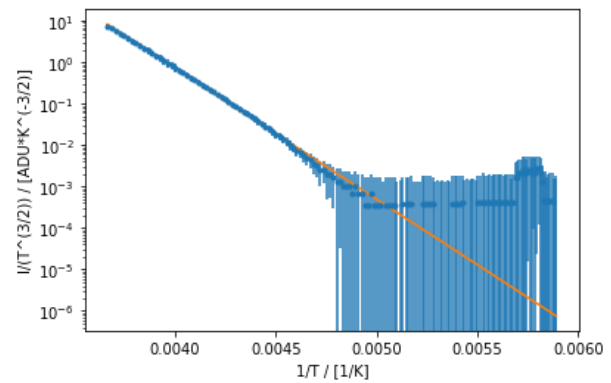


Fig.2: Dark Current Measurement, log scale, with fit

The data in the exponential part of the diagram (excluding the last data points that form a horizontal line in figure 2) was fitted using a python script (figure 2) with the function

$$I = kT^{\frac{3}{2}} e^{-\frac{E_g}{2k_B T}}$$

that describes the theoretical dependence of the dark current from the temperature. Accordingly, the band gap of the detector chip can be determined to be

$$E_g = (1.256 \pm 0.005)\text{eV}$$

The error on this experimental value of the band gap energy of the CCD detector is created in the fitting process and is relatively small. However, this experiment does not take into account that the intrinsic band gap of any material depends on the temperature. The observed shift of 100K will change the band gap energy which will increase the inaccuracy of the result. The determined bandgap is significantly higher than the band gap of silicon which is

$$E_{g,\text{Si}} = 1.15\text{eV}$$

The difference can be explained by a shift in the band gap energy due to the doping of the silicon.

Flat Field Correction

Flat-field correction describes the process of using a master flat field to improve the imaging quality by reducing the disturbing effects. For example, the individual pixels may have different sensitivities due to the manufacturing process or there may be distortions in the optical path like dust grains. A dome master flat field is an image of a structureless evenly lighted object (in our case a white surface in the telescope dome) that displays those anomalies of the detector since every pixel is illuminated with the same amount of light. For scientific observations, usually a sky flat is taken in a sky region without any bright objects. Dividing a taken picture by this master flat field will yield a corrected image that can be used for scientific purposes. In order to create flat fields for the four different filters (I,R,V and B) five images were taken each with a relatively long integration time (to achieve a good signal-to-noise-ratio) but still within the linear region of the sensitivity. Using a python script the bias value was subtracted from each of those images. Subsequently, the five images for the same filter were combined into one picture. By dividing each pixel with the median of all pixels, a normalised master flat field can be obtained. It is necessary to normalise the master flat field in order scale them towards the sensitivity of the detector. Those normalised master flat fields are shown in figure 3. The different filters each show a different detector response and therefore clearly demonstrate why it is necessary to obtain a master flat field for each filter that is used. The dips in the flat field around the $x=1000$ region probably correspond to the overscan region that joins the picture along that line. For the following analysis, the picture size will be cut accordingly so that this region is not in the analysed frame. Some of the striking signals in the 3d surface are visible in all four plots (for example, the signal at $(x=800,y=400)$) so they might belong to dead pixels or dust in the telescope that does not change when different filters are used. The clearly different shape of the flat field for the B filter is also very remarkable and might point towards an anomaly of the filter.

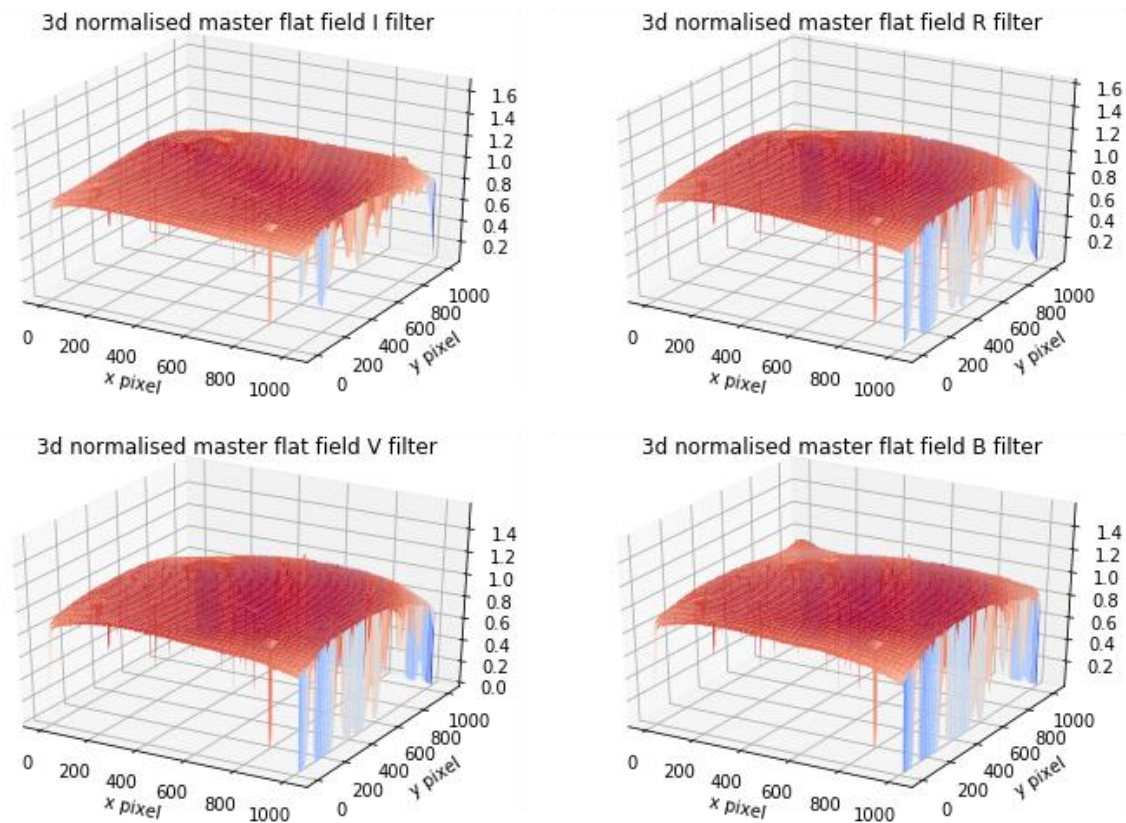


Fig.3: Normalised master flat fields

Figure 4 shows histograms of the normalised master flat fields in figure 3. All four plots show peaks around 1 which is the average sensitivity of the detector pixels. Pixels with a greater-

than-average sensitivity will have a ratio greater than 1 but as is evident from the diagrams the majority of pixels have a below-average sensitivity with a more spread-out distribution. The pixels that peak around 0 are dead pixels that do not measure any incoming light.

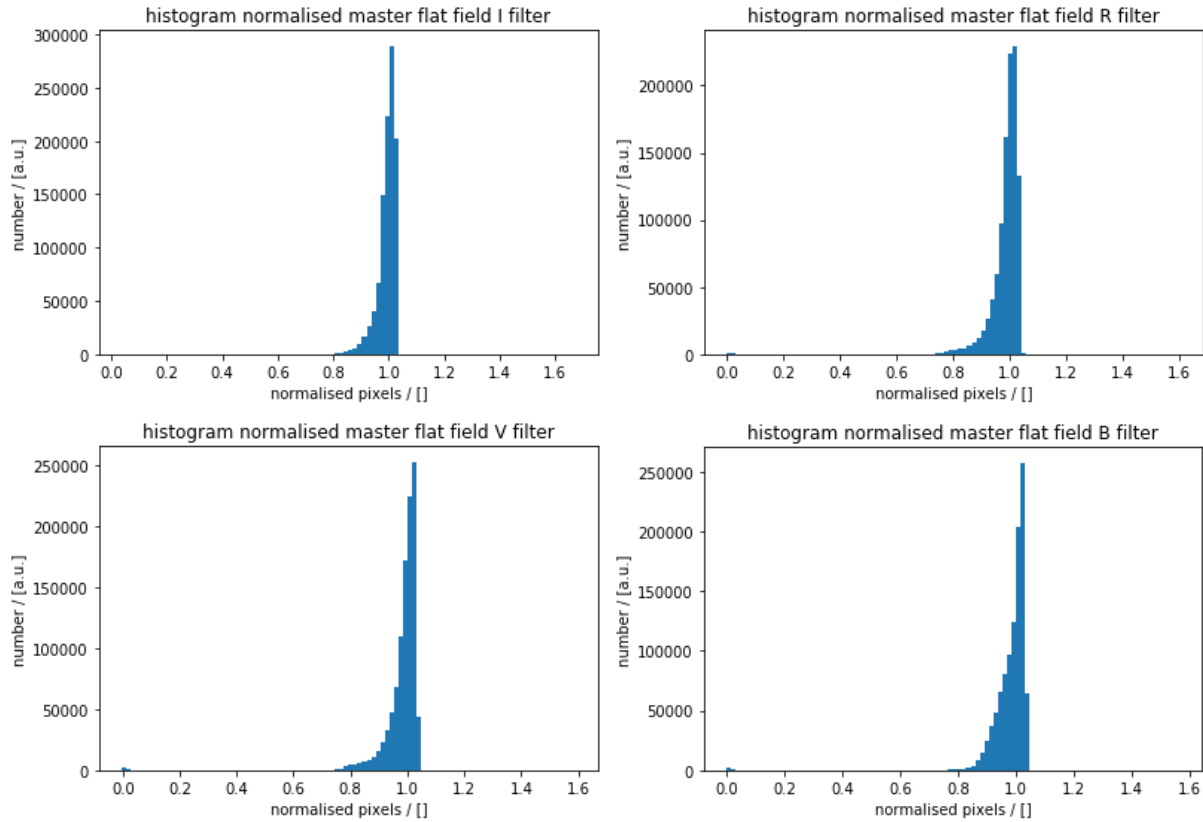


Fig.4: Histograms of the normalised master flat fields

Figure 5 shows the effect of the flat field correction: For an individual picture with the R filter the detector response before the correction is shown in blue. The surface is clearly distorted which shows that the detector has a very inhomogeneous response to the uniformly incoming light. By dividing this picture by the normalised master flat field, each pixel gets corrected and the result is a uniform detector response as expected.

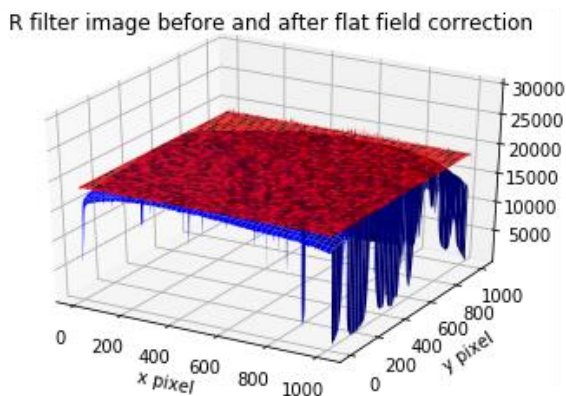


Fig.5: Flat field correction for a flat field image taken with the R filter
blue: before flat field correction
red: after flat field correction

Linearity and Dynamical Range

Ideally, the number of incoming photons onto the detector is directly proportional to the output digital signal. However, when the incoming light produces more charge carriers than the potential well is able to hold the detector gets saturated and the output signal becomes independent to the number of photons. If a single pixel gets saturated (for example when

observing a bright star with a long exposure time) the charge carriers from the potential well might flood into neighbouring potential wells, this effect is called blooming. To investigate the linear range of the used CCD camera and its limitations the detector signal is measured for different exposure times for the I and R filter. The bias value is subtracted from the individual images and a flat field correction with the normalised master flat fields determined above is performed. Then the median signal value is determined and plotted against the exposure time. The results are shown in figure 6 and 7. The linear range of the data was fitted with a linear function. The R^2 values of

$$R_I^2 = 0.99912$$

$$R_R^2 = 0.9978$$

indicate a very good agreement between the fit and the data: For the I filter the detector signal is proportional to the integration time with a 0.09% deviation, for the R filter the deviation from a perfect linear relationship is 0.2%. The strictly linear correlation between the number of incident photons and the signal is extremely important for exact measurements with the telescope. Both graphs show that the detector is saturated at approximately 65000 counts for a gain factor of 5.

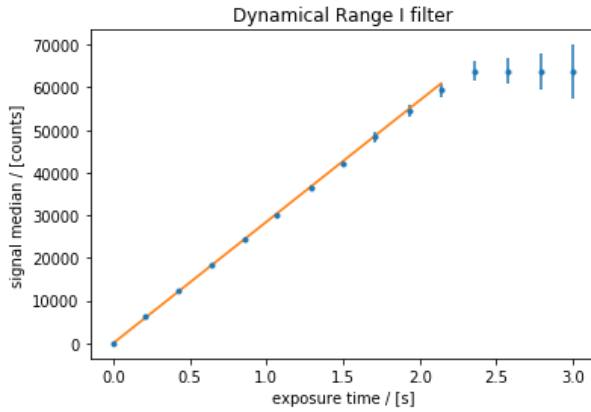


Fig.6: Dynamic Range of the detector with the I filter

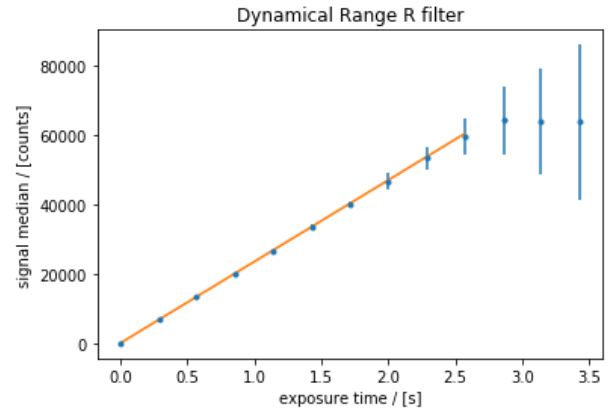


Fig.7: Dynamic Range of the detector with the R filter

Sensitivity and Noise properties

There are three sources of noise that effect the signal created by the detector: Photon noise describes the fluctuation between uniformly illuminated pixels and behaves according to Poisson statistics. The read-out noise describes the noise introduced by the read-out electronics and the Pixel Response Non-Uniformity (PRNU) noise takes into account different quantum efficiencies of pixels. The detector is also characterised by the quantum efficiency η (the efficiency with which photons are converted into electrons) and the gain κ (efficiency with which the electrons are converted into a digital output).

In the following, all three noises are determined for two pictures taken with an exposure time of 0.17s.

The noise introduced by the read-out electronics can be determined via the noise (standard deviation) in the overscan region where a uniform bias value is applied to the detector and there is no photon noise or PRNU noise. Using a python script the read-out noise of the detector can be determined as:

$$\sigma_{R,d} = (1.675 \pm 0.004) \text{ADU}$$

The photon noise can be calculated by taking the difference of two images recorded with the same exposure time. The PRNU noise cancels in the difference picture as it is purely dependent on the number of incoming photons. The photon noise can then be determined:

$$\sigma_{\text{diff}}^2 = 2(\sigma_{\text{R,d}}^2 + \sigma_{\text{e,d}}^2)$$

$$\sigma_{\text{e,d}} = 23.9\text{ADU}$$

Using the error calculation for the total noise

$$\sigma_{\text{total}}^2 = \sigma_{\text{R,d}}^2 + \sigma_{\text{e,d}}^2 + \sigma_{\text{PRNU,d}}^2$$

the PRNU noise can be determined as

$$\sigma_{\text{PRNU,d}} = 76.9\text{ADU}$$

The PRNU noise is the biggest contributor to the total noise followed by the photon noise; the read-out noise is significantly smaller than those two uncertainties. Since the read-out noise is only limited by the manufacturing quality it can be set to a level where it does not affect the quality of the images. The PRNU noise and the photon noise are connected to each other, typically, the photon noise dominated at small electron levels (low light intensities or short exposure times) whereas the PRNU noise that is connected to different quantum efficiencies of the pixels dominates at higher signal levels.

The gain of the CCD camera can be determined using

$$\sigma_{\text{diff}}^2 = 2(\sigma_{\text{R,d}}^2 + \frac{N_{\text{e,d}}}{\kappa})$$

In figure 8 the variance of the difference picture is plotted against the median intensity. Using the read-out noise determined above the gain can be determined by a linear fit to be

$$\kappa = 10.5 \pm 0.2$$

Only the first data points were used for the fit. The drop in the variance of the difference picture in figure 8 can be explained by the detector beginning to get saturated.

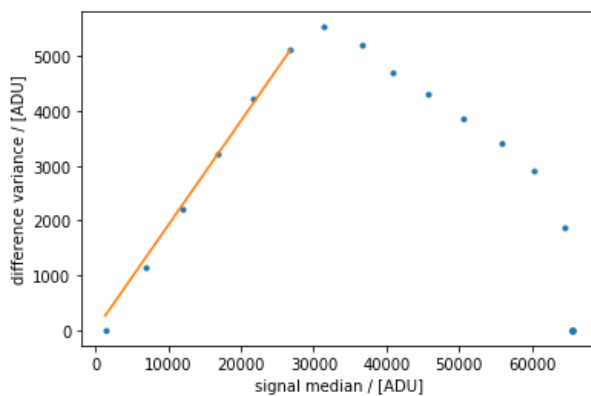


Fig.8: Determination of the gain of the CCD camera

The gain can also be calculated assuming a Poisson-shape of the photon noise

$$\sigma_{\text{e,d}}^2 = \frac{\eta}{\kappa} N_{\text{e,d}}$$

and a quantum efficiency of $\eta=1$. The value of

$$\kappa = 10.481 \pm 0.006$$

is within one standard deviation of the gain determined above, the discrepancy is not statistically significant and the value determined above can be confirmed. In those calculations the quantum efficiency of the detector is assumed to be perfect which in reality is not the case.

Investigating the quantum efficiency and taking it into account for the performed calculations will significantly improve the quality of the results.

Part II: Photometry of globular clusters

Zeropoint calibration

Before starting the actual photometry, we first have to calibrate the two images of the BS90 globular cluster. In order to do so we compared the counts of the standard stars in the Hubble images with their known apparent magnitudes from the catalogue SIMBAD. Using the following formula, we then calibrated the individual zeropoints.

$$\text{Zeropoints} = m_{\text{Catalog}} + 2.5 \log_{10}(\text{counts})$$

By applying the Gaussian Error propagation we received an error of

$$\text{Zeropoint_err} = 2.5 \text{counts}_{\text{err}} / (\text{counts} * \ln(10))$$

Calculating the median of both the values for the zeropoint and there errors we determined

$$\text{zeropoint}_V = 25.124 \pm 0.03$$

$$\text{zeropoint}_I = 25.049 \pm 0.017$$

As expected by Planck's radiation Law the value in the visual is larger than the one in the infrared range.

PSF photometry with python

In order to determine the point spread functions of the respective filters we firstly determined approximately 40 different stars in each image that are not overlapping with other stars, are bright enough and do not saturate the CCD (Fig9 and Fig 10):

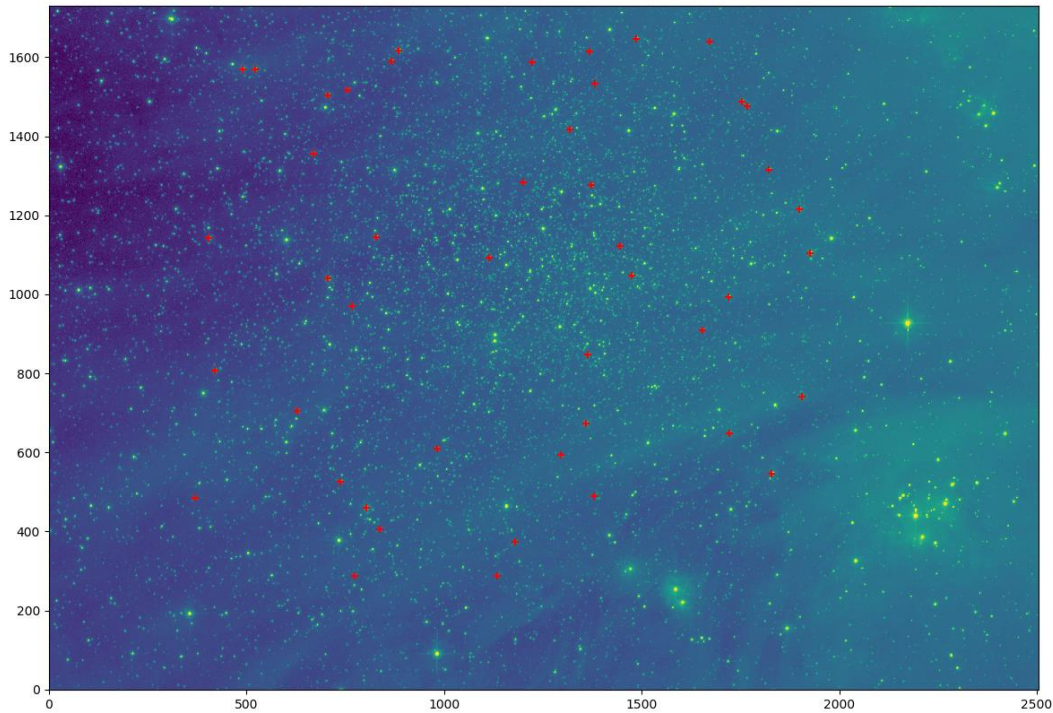


Fig.9: Selected stars for the PSF in the V-Band (x and y axis are pixels)

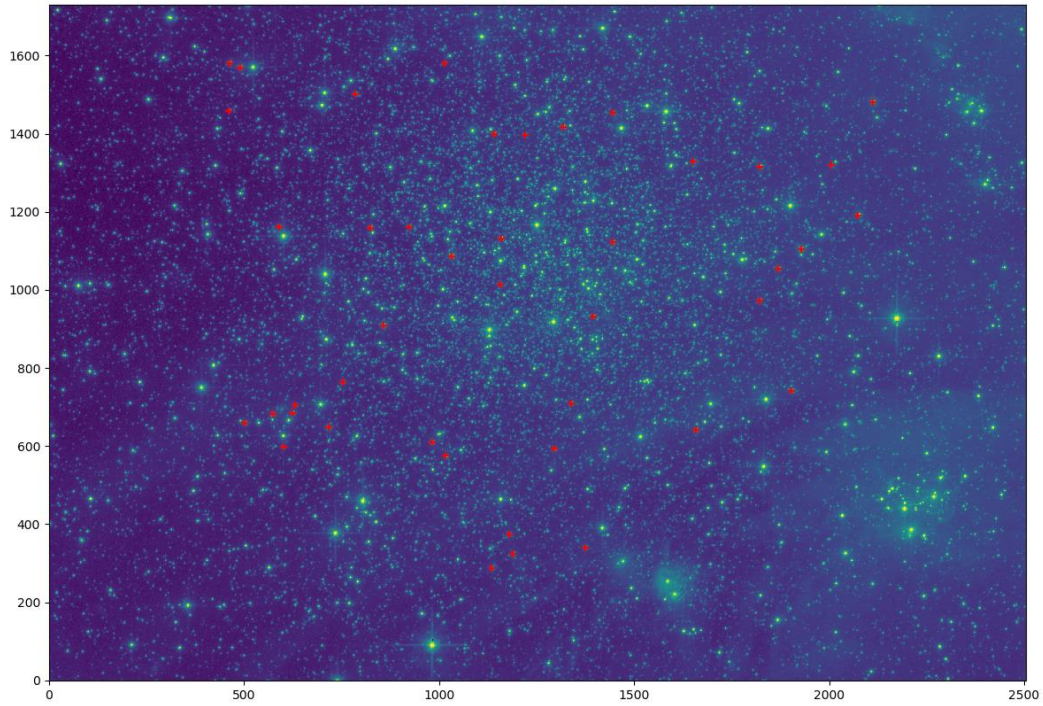


Fig.10: Selected stars for the PSF in the I-Band (x and y axis are pixels)

After closer evaluating the stars in a zoomed-in frame in regard to whether they really fit the criteria for creating a point spread function the remaining stars were then used to create that PSF:

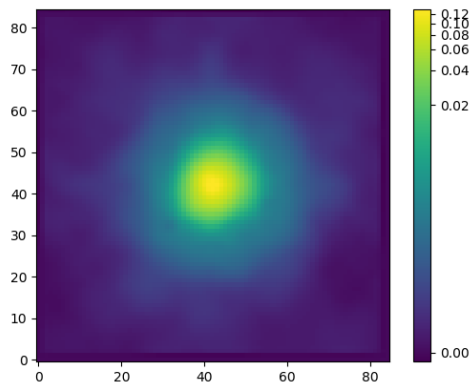


Fig.11: PSF for the stars in the V-Band (x and y axis are pixels)

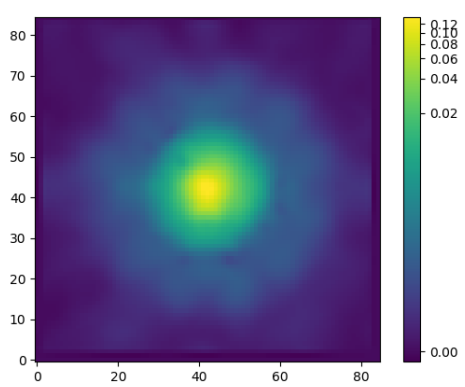


Fig.12: PSF for the stars in the I-Band (x and y axis are pixels)

Though we could not determine an error of these PSFs one can see that they show minor irregularities in comparison to an angular symmetric PSF based on Poisson statistics. These irregularities might be caused by other stars that were close to the chosen stars and thereby impacting the PSF.

Using these PSFs we then performed the iterative PSF photometry by finding the stars in the Hubble images that fit the respective PSFs and marking them in that image:

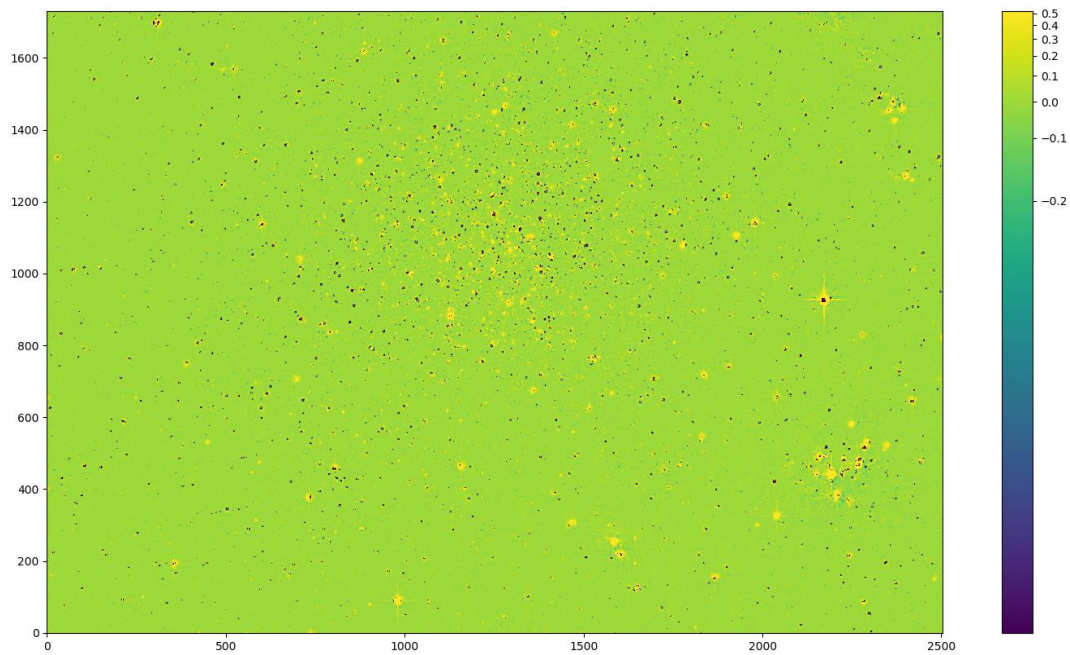


Fig.13: Iterative PSF Photometry of the image in the V-Band (x and y axis are pixels)

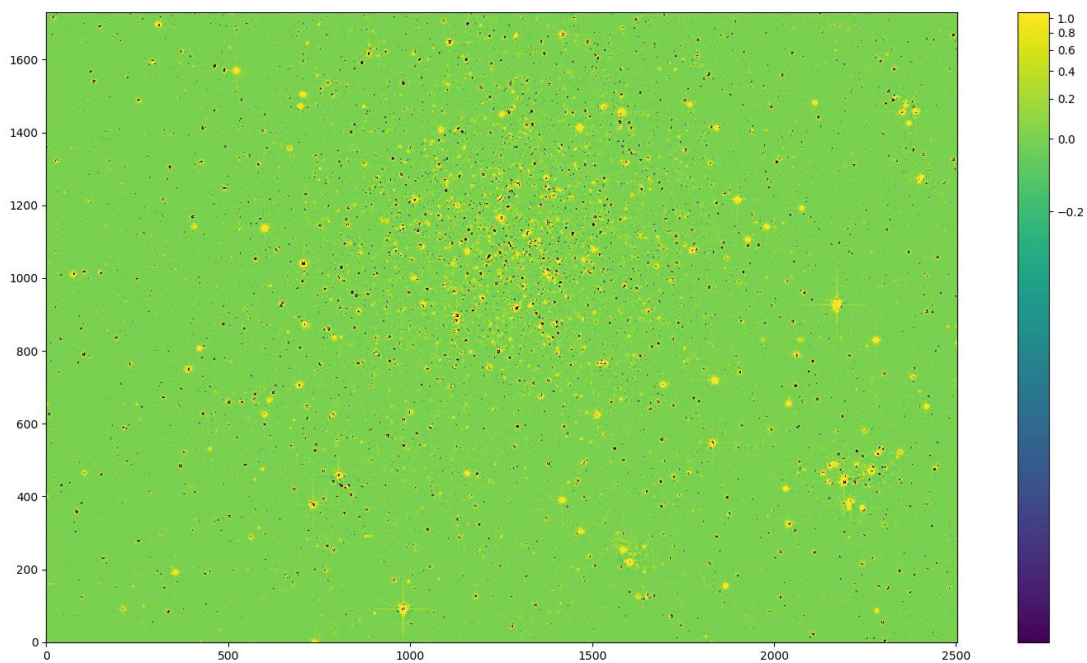


Fig.14: Iterative PSF Photometry of the image in the I-Band (x and y axis are pixels)

In both pictures the determined star positions match the star positions in the image. However not all of the stars were found. This might be because the not determined stars are either really big stars and therefore do not fit the PSF model as in the radius of the PSF model they are completely or almost completely saturated or they are really close to other stars or hidden in nebular or dust. In both cases the almost angular symmetry is not given which is why the stars could not be identified by the PSF.

Additionally, the negative values are due to the fact that the iterative photometry was performed using the *IterativelySubtractedPSFPhotometry* – class of *photutils* which is a part of the *astropy* package of python. The class performs the photometry by initially finding sources from which it creates a model that is then subtracted from the image. This subtraction may result in negative values in the image as the PSF's maximum is a median of all the selected stars

thereby being larger than 50% of the selected stars which were the brighter ones. Hence all the negative spots in Figure14 mark positions of stars.

Color-Magnitude-Diagram

In a Color-Magnitude-Diagram the absolute magnitude of a star or a group of stars is plotted over the color index which is in our case the difference between the V-Band and the I-Band as opposed to the Hertzsprung-Russel-Diagram (HRD) where the absolute magnitudes are plotted over the spectral class. The advantage of the Color-Magnitude-Diagram is that it is similar to the HRD but at the same time is the main sequence vertically dislocated depending on the distance to the observed stars. Thus, the CMD allows for a direct determination of the distance from the observed objects to the observer. Additionally, by overplotting isochrones in the CMD one can also determine the metallicity and age of the stars involved. In our case that leads us to the following diagrams:

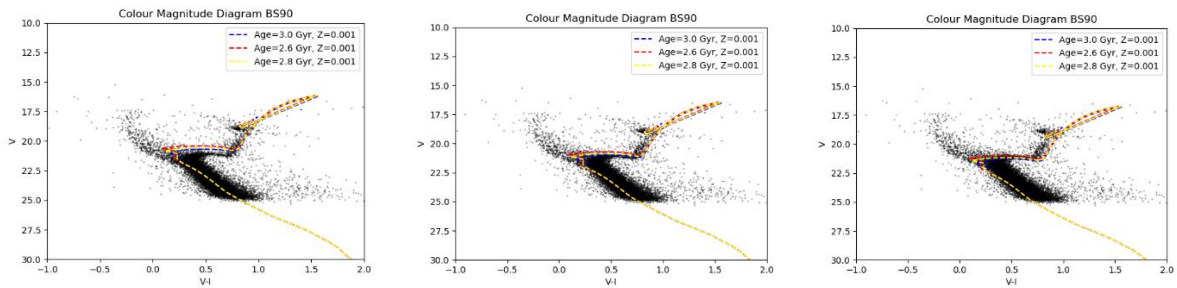


Fig.15: CMD of BS90 for a magnitude offset of 18.7,19,19.3 from left to right

By comparing the different magnitude offsets, we figured that an offset of $dY = 19 \pm 0.3$ fits best to the data. Using the formula (again with Gaussian error propagation for the error)

$$d = 10^{\frac{dY+5}{5}} \text{ and } d_{\text{err}} = \ln(10) * 5^{\frac{dY}{5}} * 2^{\frac{dY+5}{5}} * dY_{\text{err}}$$

we derive a distance of $d = 63095 \pm 148 \text{ pc}$. Comparing this to the literature value of $d_{\text{lit}} = (58.9 \pm 0.45) \text{ kpc}$ we can see that our determined value differentiates significantly from the literature value ($\approx 34\sigma$). However, our determined error might have been too slim. If we consider an error of $dY_{\text{err}}=1$ we arrive at $d = 63095 \pm 738 \text{ pc}$ which is still significantly different ($\approx 7\sigma$) but more reasonable.

To determine the age and metallicity of BS90 we set a magnitude offset of 19:

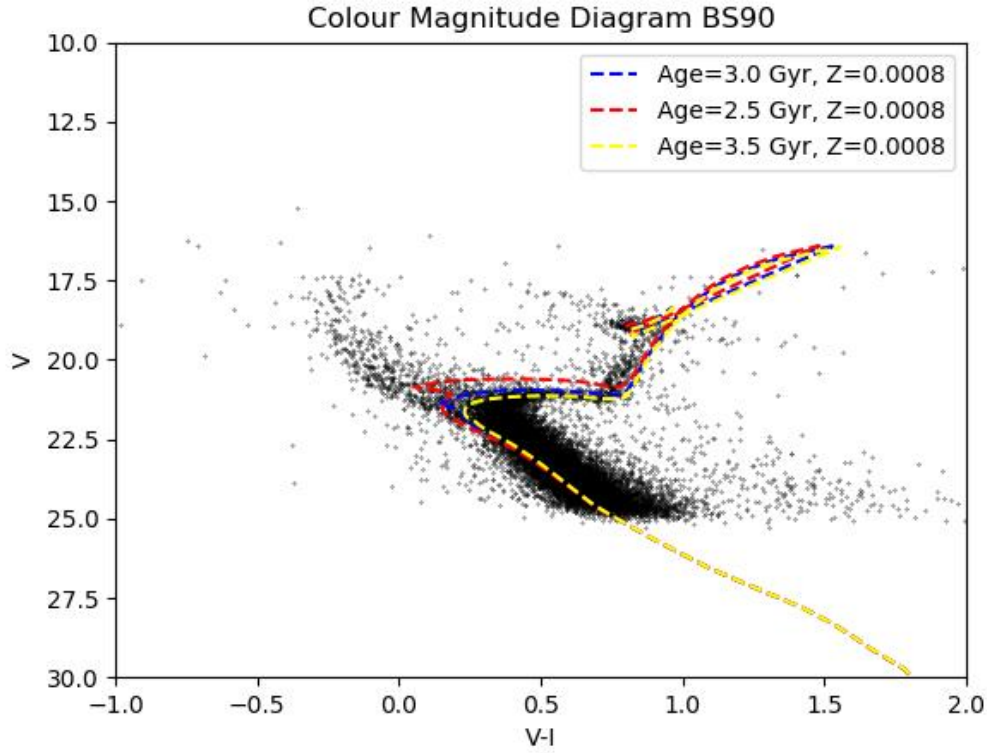


Fig.16: CMD of BS90 at a magnitude offset of 19 and different ages

Comparing different isochrones to our data we determined the age to be 3.0Gyr with an error of 0.5Gyr corresponding within 3σ to the literature value of 4.5Gyr.

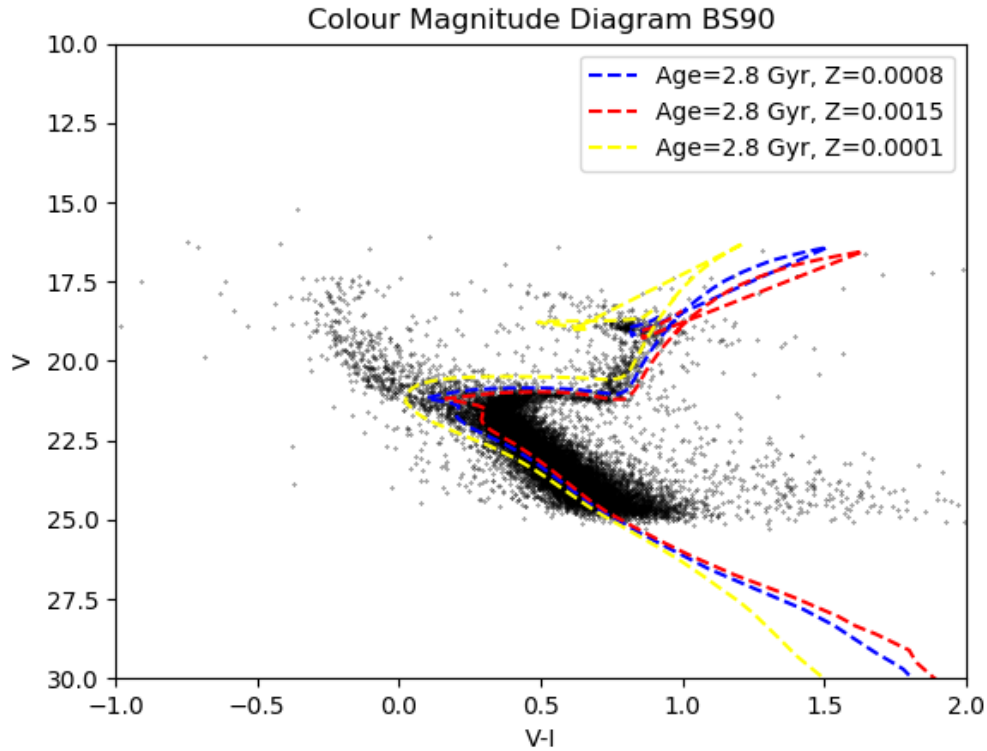


Fig.17: CMD of BS90 at a magnitude offset of 19 and different metallicities

Again, using isochrones, we determined a metallicity of $z = 0.0015 \pm 0.0007$ which differentiates significantly to the literature value of 0.004 which is why we assume we underestimated our error.

In conclusion we determined BS90 to be 3.0Gyr old, have a metallicity of 0.0015 and be 63.1kpc away. Our biggest error lies probably in the fact that we firstly looked at different ages and metallicities trying to find an isochrone that fits our data while keeping the magnitude offset fixed. A more efficient way might have been to first determine the magnitude offset and then differentiating the metallicities and ages as the offset is best to be determined in a way that the isochrone passes where the most main sequence stars are found while the metallicity and age modulate the 'arm' of the isochrone. Nevertheless, we were surprised on how accurate one is able to determine all these properties of the globular cluster by 'just' comparing to images to one another.